AIAA JOURNAL
Vol. 58, No. 12, December 2020

Effects of Engine Acoustic Waves on Aerooptical Environment in Subsonic Flight

Stanislav Gordeyev* and Matthew Kalensky†
University of Notre Dame, Notre Dame, Indiana 46556

https://doi.org/10.2514/1.J059484

Spatially and temporally resolved wave fronts were collected in flight using Airborne Aero-Optics Laboratory at varying subsonic Mach numbers through both the naturally developing boundary layer and an artificially generated shear layer. Dispersion analysis was used to separate the wave fronts into the downstream and upstream-traveling components. The upstream propagating component was associated with sound waves, originating from the aircraft's engine, located downstream of the measurement location, with convective speeds that are consistent with theoretical predictions. The spectra of the acoustic-related component were dominated by the tonal frequency associated with the engine's fan blade pass frequency. Modal analysis also revealed the streamwise spatially periodic nature of the acoustic component of the wave fronts, further confirming the acoustic nature of these distortions. An analytical model was derived which established the relationship between overall levels of acoustic-related optical distortions and the acoustic pressure fluctuations. The model was used to estimate the acoustic pressure spectra and sound pressure levels at the measurement location.

Nomenclature

A	=	amplitude coefficient
c	=	speed of sound
D	=	beam diameter
f	=	frequency
G	=	aperture function
K_{GD}	=	Gladstone–Dale constant
k	=	index
k_x, k_y	=	wave numbers
L	=	distance between engine and measurement location
M	=	Mach number
n	=	index of refraction
OPD	=	optical path difference
P_{ref}	=	reference pressure to compute sound pressure level
p	=	pressure
R^*	=	modified distance, defined in Eq. (8)
S	=	autospectral density function
SPL	=	sound pressure level
St	=	Strouhal number
T	=	block duration
t	=	temporal coordinate
U	=	velocity
x, y, z	=	spatial coordinates
η	=	parameter, defined in Eq. (13)
Λ	=	structure size
Λ_{SL}	=	shear-layer structure size
λ	=	laser wavelength
ξ	=	parameter, defined in Eq. (11)
ρ	=	density
φ	=	dynamic mode decomposition mode
ϕ	=	parameter, defined in Eq. (11)

Subscripts

A	=	aperture frame of reference
BP	=	blade pass
C	=	convective value
RMS	=	root mean square
∞	=	freestream value

Superscripts

Down	=	traveling downstream
Up	=	traveling upstream
‘	=	fluctuating value
$-$	=	time-averaged
$\langle\rangle$	=	spatially averaged

I. Introduction

THE propagation of a laser beam through a field of varying index of refraction leads to temporally changing aberrations imposed onto the initially undistorted wave fronts [1,2]. These changes in the index of refraction are the result of changes in the local density as described by the Gladstone–Dale relation shown in Eq. (1),

$$n' = K_{\mathrm{GD}}\rho' \tag{1}$$

At relatively high subsonic speeds, the density fluctuations are due to compressibility effects and pressure variations inside the large-scale turbulent structures. The related aerooptical effects have been extensively studied over the last few decades; see the review papers [1,2], for instance.

Another source of density fluctuations is acoustic waves, radiating either from a tunnel motor for the case of wind tunnel testing or from the aircraft engine as will be shown in this Paper. Acoustic waves can be described as isentropic pressure fluctuations, which travel at the speed of sound. From the definition of the speed of sound, pressure fluctuations are related to density fluctuations by Eq. (2),

$$c = \sqrt{(\partial p/\partial \rho)_S} = \sqrt{p'/\rho'} \tag{2}$$

Consequently, if a laser propagates through an acoustic environment, the density fluctuations imposed by the acoustic waves will distort the laser beam. These acoustic-related distortions will be added to the flow-related aerooptical distortions. Consequently, in environments where both sources of aberrations are present, such as airborne laser systems, overall higher levels of distortions are measured, and the

Presented as Paper 2019-3253 at the AIAA Aviation Forum, Dallas, TX, June 17–21, 2019; received 3 February 2020; revision received 4 June 2020; accepted for publication 5 June 2020; published online 26 June 2020.

*Associate Professor, Department of Aerospace and Mechanical Engineering, 113 Hessert Laboratory for Aerospace Research. Associate Fellow AIAA.

†Graduate Research Assistant, Department of Aerospace and Mechanical Engineering, B036 Hessert Laboratory for Aerospace Research. Student Member AIAA.

coupling of acoustic and flow-related distortions should be taken into account. In both wind tunnel and flight tests, the acoustic contamination introduces a corrupting effect and should be properly removed from the experimental data, if investigating aerooptical effects due to the turbulent flows is the primary interest [3–5].

The corrupting effect of acoustic waves was first noticed in flight-test data reported in [6], in which atmospheric temperature measurements were collected and analyzed. The effect was observed as upstream-traveling waves of a very specific frequency appeared to propagate at a fraction of the speed of sound. It was suggested and confirmed that these periodic, upstream-traveling structures were attributed with the screech-type noise radiating from the engine exhaust. More recently, aerooptical effects of acoustic waves emanating from a jet engine fan in flight were directly observed and preliminarily studied in [7]. It was shown that acoustic radiation in the form of sound waves traveling upstream from the aircraft engine introduces appreciable spatial and temporal wave front variations on the laser beam.

The work discussed here further investigates the distortions imposed by acoustic waves from the engine fan on a laser beam in-flight, using the Airborne Aero-Optics Laboratory - Beam Control (AAOL-BC). The primary objective of AAOL-BC is to provide an in-flight testing platform where aerooptics experiments can be performed under real conditions. AAOL-BC campaigns, along with campaigns from predecessor programs AAOL [8] and AAOL-Transonic (AAOL-T) [9], have been an integral part of advancing current understanding of aerooptical interactions. It remains an instrumental program for acquisition of experimental data in realistic aerooptical flowfields [10–12], as well as for studying effects of flow control devices on aerooptical performance.

The experimental work presented here investigates the aeroacoustic environment measured using a wave front sensor in flight under two different flow conditions over the same measurement location at various subsonic and transonic speeds. The two different conditions include the naturally developing boundary layer over the optical window as well as a shear layer generated by attaching a porous fence to the aircraft fuselage upstream of the optical window. This Paper decouples the acoustic- and aerodynamic-related distortions and focuses specifically on quantifying the acoustic-related aerooptical effects at different flight conditions. In addition, an analytical relationship between the amplitude of the acoustic pressure waves and the resultant acoustically induced optical aberrations is derived, and the experimental results are compared with the analytical model.

II. Experimental Setup

The experiments were performed with AAOL-BC. AAOL-BC consists of two Falcon-10 aircraft flying in close formation, nominally 50 m apart. One of the aircraft, designated as the source aircraft, projects a 532 nm diverging laser beam onto a custom-designed optical quality window mounted on the second aircraft, referred to here as the laboratory aircraft. The window, shown in Fig. 1, left plot, has a clear aperture 0.3048 m in diameter, with an optical quality of better than $\lambda/10$ in surface flatness. The window is mounted on a specially designed aluminum mount, meant to limit distortions to the attached boundary layer as fluid convects from the aircraft fuselage over the window. Detailed measurements of the boundary layer profiles over the optical window are presented in [13], and it was found that the boundary layer is sufficiently close to being considered canonical, with the total thickness of about 50 mm at the tested Mach numbers. All measurements taken through the turbulent boundary layer over the window will be referred to as the boundary-layer (BL) cases.

To create a shear layer over the window, a porous fence was installed directly upstream of acquisition window on the laboratory aircraft as seen in Fig. 1, right plot. In previous experimental studies, porous fences were shown to create shear layers by slowing the flow downstream of the fence via turbulence-related total pressure losses [14]. The fence has a semicircular shape with a radius of 0.152 m and is installed normal to the aircraft surface on a mounting bracket, upstream of the acquisition window. The fence had a porosity coefficient of 0.4, defined as the area of open holes in the fence divided by the total fence area. The aerooptical environment caused by the shear layer, formed by the fence, is discussed in detail in [13,15]. It was found that the measured data were dominated by the presence of the large-scale structures elongated in the spanwise direction. All measurements with the turbulent shear layer over the window will be referred to as the shear-layer (SL) cases.

To measure aerooptical distortions imposed on the incoming laser beam, the laboratory aircraft was equipped with a beam stabilizing system, reimaging optical components and a high-speed Shack–Hartmann wave front sensor (SHWFS). The optical setup is illustrated in Fig. 2. Both planes were positioned such that the incoming beam is approximately normal to the flat window. To stabilize the incoming beam, a computer-controlled proportional feedback system was employed. The system consists of a tracking camera, a mirror controller, and an Aerotech gimbal with a flat mirror (0.3 m in diameter). The tracking camera collects images at 150 frames/s and computes relative image displacements in both horizontal and vertical directions, using a frame grabber and National Instruments (NI) Labview software. The software is capable of analyzing approximately 600 frames/s. Using these computed displacements, the mirror controller commands azimuthal and elevation motors on the gimbal to compensate for these angular differences. As the controller output is still much faster than the response of the stepper motors, a five-frame averaging filter is used in the output signal to smooth stepper motor motion. Thus, the estimated frequency response of the closed-loop tracking system is about 30 Hz, which was deemed sufficient to compensate for a slow relative motion of both aircraft.

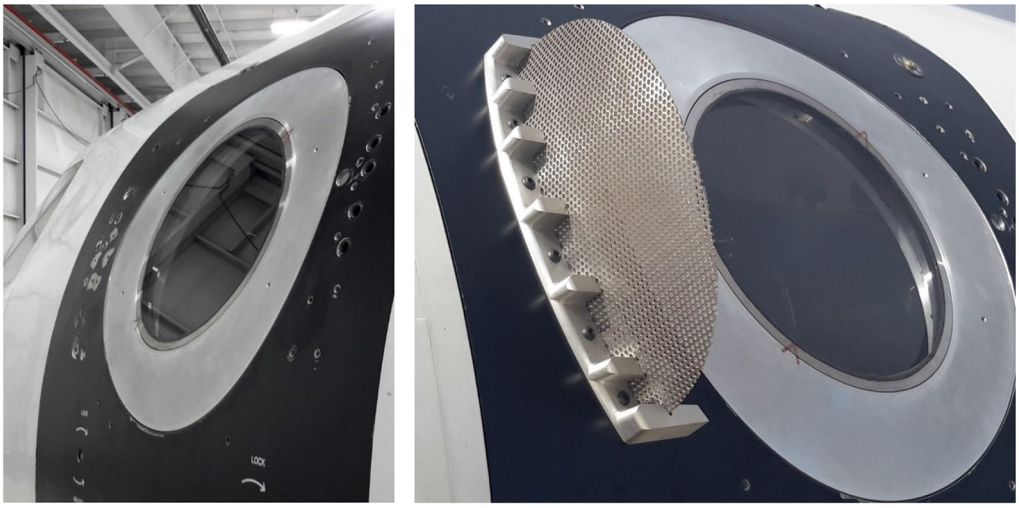

Fig. 1 Left: Flat window for boundary-layer tests. Right: Perforated plate installed in front of the flat window for shear-layer studies.

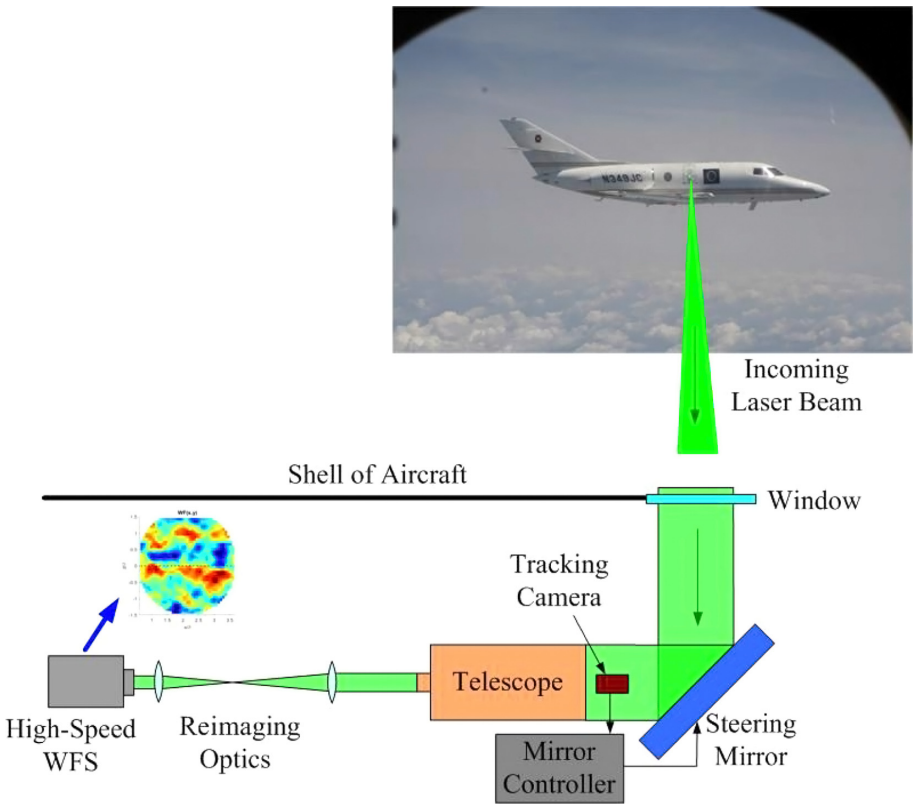

Fig. 2 The optical setup and acquisition system on the AAOL-BC.

Table 1 Flight parameters for different flow conditions over the window

Tested cases	Flight Mach numbers	Altitudes, m	Freestream temperatures, K
Boundary layer	$M_\infty = 0.4, 0.5, 0.6, 0.7$	4877	251
Shear layer	$M_\infty = 0.5, 0.6, 0.7$	5182 and 5791	264 and 260

After the incoming laser beam was stabilized, a Schmidt–Cassegrain telescope with a diameter 203 mm and a central obscuration 64 mm in diameter, coupled with several lenses, was used to contract an incoming circular beam with $D = 203$ mm to a collimated beam (16 mm in diameter). This beam was then forwarded to the SHWFS. The SHWFS has a spatial resolution of 50×50 subapertures, each 0.3 mm in size, allowing the aberrations imposed on the laser beam wave fronts to be measured with great spatial accuracy. Wave fronts were acquired at different sampling frequencies between 25 and 50 kHz, typically producing approximately 30,000 frames per collection.

AAOL-BC's two Falcon-10 aircraft were flown between $M_\infty = 0.4$ and 0.7 at altitudes between 4877 and 5791 m; see Table 1 for flight conditions. The freestream temperatures were measured using aircraft instrumentation.

Falcon-10 aircraft has one engine on each side of the fuselage. The aircraft engine was located $L = 4.4$ m downstream of the measurement window, with the engine axis offset 0.54 m away from the aircraft fuselage. At maximum engine throttle, the 30 blade Honeywell TFE-731-2-1C engine fan rotates at a speed of 11, 502 rotations/min. During experiments, the percent of maximum throttle at each Mach number was recorded allowing the blade pass frequency f_{BP} associated with each Mach number to be calculated.

III. Wave Front Data Reduction

The SHWFS uses an array of lenslets to focus the incoming light source to points on a digital Complementary metal–oxide–semiconductor (CMOS) sensor. The deviation of the points from their respective center locations allows for the calculation of local average slopes over the discrete spatial areas corresponding to each lenslet. Using a Southwell reconstructor, these measured slopes $\theta(x_A, y_A t)$ can be used to calculate the spatially and temporally changing optical path differences (OPDs) $\mathrm{OPD}(x_A, y_A t)$; wave fronts are commonly approximated as negative OPDs [16]. Here, x_A and y_A are aperture-related spatial coordinates.

The root mean square (RMS) of the OPD in space is a measure of the wave front's time-dependent departure from planarity, as shown in Eq. (3),

$$\mathrm{OPD}_{\mathrm{RMS}}(t) = \sqrt{\langle \mathrm{OPD}(x_A, y_A, t)^2 \rangle_{x_A, y_A}} \tag{3}$$

Here, the brackets denote averaging over the aperture spatial coordinates. The $\mathrm{OPD}_{\mathrm{RMS}}$ refers to the time-averaged RMS of the OPD and elicits the average degree of wave front aberrations. The time-averaged $\mathrm{OPD}_{\mathrm{RMS}} = \overline{\mathrm{OPD}_{\mathrm{RMS}}(t)}$ is the most common metric to quantify the degree of distortion associated with an aerooptical environment.

If a typical spatial scale of the optical distortions on a beam is larger than the diameter of the viewing aperture, the resultant distortions will see a net deflection of the beam, known as tip/tilt. However, mechanical vibration inevitably corrupts the slope measurements also in the form of tip/tilt. Therefore, typically before performing any data reduction procedures on the experimentally measured reconstructed wave fronts, the instantaneous tip, tilt, and piston are removed from the data. If the optical distortions are smaller than the aperture, there will be no appreciable tip/tilt present in the wave fronts. Thus, the aperture acts as a form of a spatial filter [16]. Understanding this concept will be important in the later discussion.

To decouple flow-related aerooptical and aeroacoustically induced distortions, dispersion analysis and dynamic mode decomposition (DMD) were employed. The utility of these approaches will be described in detail in the following.

A. Dispersion Analysis

At subsonic speeds in the aircraft frame of reference, acoustic waves travel upstream, opposite the direction of the convective

turbulent structures. A dispersion analysis was applied to the spatial-temporal wave fronts, as it is effective at identifying and separating upstream-moving acoustic and downstream convecting (boundary- or shear-layer-related) optical disturbances. This approach transforms a three-dimensional wave front dataset $\mathrm{OPD}(x_A, y_A, t)$ into the wave-number-frequency domain using a three-dimensional Fourier transform and computes a three-dimensional autospectral density function or a power spectrum $S_{\mathrm{OPD}}(f, k_x, k_y)$ as described by Eq. (4),

$$\widehat{\mathrm{OPD}}(f,k_x,k_y) = \int_{-\infty}^{\infty}\int_{-\infty}^{\infty}\int_{-\infty}^{\infty} \mathrm{OPD}(t,x,y)e^{-i(2\pi f t - k_x x_A - k_y y_A)}\,\mathrm{d}t\,\mathrm{d}x\,\mathrm{d}y$$
$$S_{\mathrm{OPD}}(f,k_x,k_y) = \frac{\left|\widehat{\mathrm{OPD}}(f,k_x,k_y)\right|^2}{T\cdot D^2} \tag{4}$$

As both acoustic and convective structures move mostly in the streamwise direction, for simplicity, the power spectrum can be further integrated in the spanwise direction to obtain a two-dimensional projection of the power spectrum,

$$S_{\mathrm{OPD}}(f,k_x) = \int_{-\infty}^{\infty} S_{\mathrm{OPD}}(f,k_x,k_y)\,\mathrm{d}k_y \tag{5}$$

The traveling structures correspond to lines $2\pi f t - k_x x_A = \text{const}$. Consequently, the traveling structures of various frequencies would appear in the spectrum as branches with constant slopes. The slope indicates the value and, more importantly, the sign of the convective velocity as $U_C = 2\pi f / k_x$.

B. Dynamic Mode Decomposition

To further study the downstream and upstream moving structures, a dynamic mode decomposition [17,18] was used to decompose the wave fronts into a series of spatial modes and corresponding coefficients, as shown in Eq. (6). Various algorithms are available to compute DMD modes; see [17], for instance. In particular, in [19], it was demonstrated that when a temporal mean is subtracted from the data, then DMD is reduced to a temporal discrete Fourier transform (DFT). As the mean was removed from the collected wave fronts, DMD modes, later called dynamic modes, in our case can be computed by performing DFT at every spatial point, as described in [19]. Both traditional [17] and DFT algorithms were implemented by the authors, and it was found that the DFT algorithm provides the same results as using the traditional algorithms, but with great computational savings. The aperture-averaged wave front power spectra for the corresponding upstream- and downstream-moving components $S^{\{\mathrm{Up/Down}\}}(f)$ were also computed as the aperture-averaged squares of the modes' amplitudes; see Eq. (6). Here, the angle brackets again denote the aperture-averaging:

$$\mathrm{OPD}^{\{\mathrm{Up/Down}\}}(t,x_A,y_A) = \sum_k \exp(2\pi i f_k t)\phi_k^{\{\mathrm{Up/Down}\}}(x_A,y_A;f_k)$$
$$S^{\{\mathrm{Up/Down}\}}(f_k) = \left\langle \left|\phi_k^{\{\mathrm{Up/Down}\}}(x_A,y_A;f_k)\right|^2 \right\rangle_{x_A,y_A} \tag{6}$$

IV. Results and Discussion

A. Experimental Data Analysis

Representative consecutive wave fronts for the BL case at $M_\infty = 0.4$ are presented in Fig. 3. The wave fronts show small-scale spatial optical distortions traveling in the direction of the flow, typical of a turbulent boundary layer (TBL). Upon closer inspection, the wave front time series seems to also contain upstream-traveling spanwise-uniform, periodic structures, indicated by the arrows in Fig. 3.

The porous fence, shown in Fig. 1, right plot, introduced a velocity mismatch by slowing the flow downstream of the fence, which formed a shear layer over the measurement window. The representative wave fronts collected for the $M_\infty = 0.5$ shear-layer case are shown in Fig. 4. The large, periodic optical distortions are clearly observed. The amplitudes of the aerooptical distortions are significantly larger for the shear layer, compared to the boundary-layer case, shown in Fig. 3. The structures are elongated in the cross-stream y direction, indicating pseudospanwise uniform structures. These distortions are due to localized regions of lower pressure (and consequently, lower density) inside the vortical structures. The regular vortical structures, characteristic of shear layers, are caused by an inflection instability mechanism [20]. In [13], the streamwise structure size for the shear layer Λ_{SL} was calculated and was found to be $\Lambda_{\mathrm{SL}} = 0.133$ m for the $M = 0.5$ case, $\Lambda_{\mathrm{SL}} = 0.137$ m for $M = 0.6$ case, and $\Lambda_{\mathrm{SL}} = 0.14$ m for $M = 0.7$ case.

The two-dimensional dispersion power spectra for the boundary-layer case and for all Mach numbers are presented in Fig. 5. In each subplot, three distinct branches are observed. One broadband branch is located in the upper, positive-frequency region, corresponding to the downstream-convecting structures inside the boundary layer. Most of the spectral energy is associated with this boundary-layer-related branch. The slope of this branch gives a convective speed of the underlying aerooptical structures. In previous studies [3], the convective speed of aerooptical subsonic boundary-layer structures was found to be approximately 0.82 of the freestream speed. A solid line corresponding to this convective speed is also plotted in Fig. 5. This line agrees with the location of the local spectral maxima, indicating that the aerooptical structures of the in-flight boundary layer indeed convect at this speed.

Another weaker branch can be observed in the lower, negative-frequency region. This branch is related to the acoustic waves originating from the aircraft engine fan and traveling upstream. The dashed line represents the expected speed of the optical distortions due to the acoustic waves, $U_C = c - U_\infty = c(1 - M_\infty)$, where c is the freestream speed of sound. This line also agrees well with the branch slope at all Mach numbers.

During the data collection, the aircraft had inevitable slow drift in a relative separation, resulting in slowly changing defocus present in

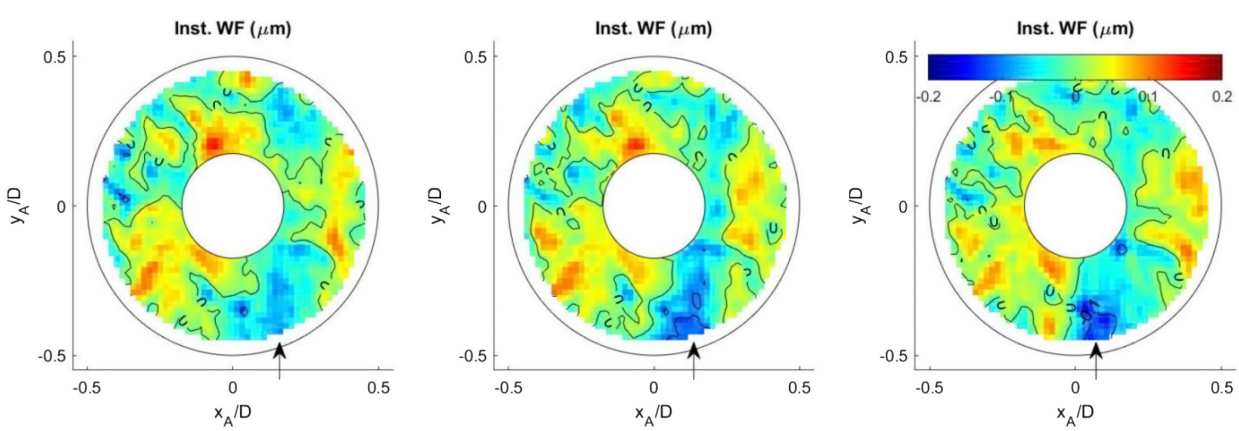

Fig. 3 Consecutive instantaneous wave fronts (labeled as Inst. WFs) for the BL case. Spatial coordinates are normalized by the beam diameter, $D = 0.2$ m. Incoming $M_\infty = 0.4$, flow goes from left to right. Arrows on each plot indicate the structure, moving upstream.

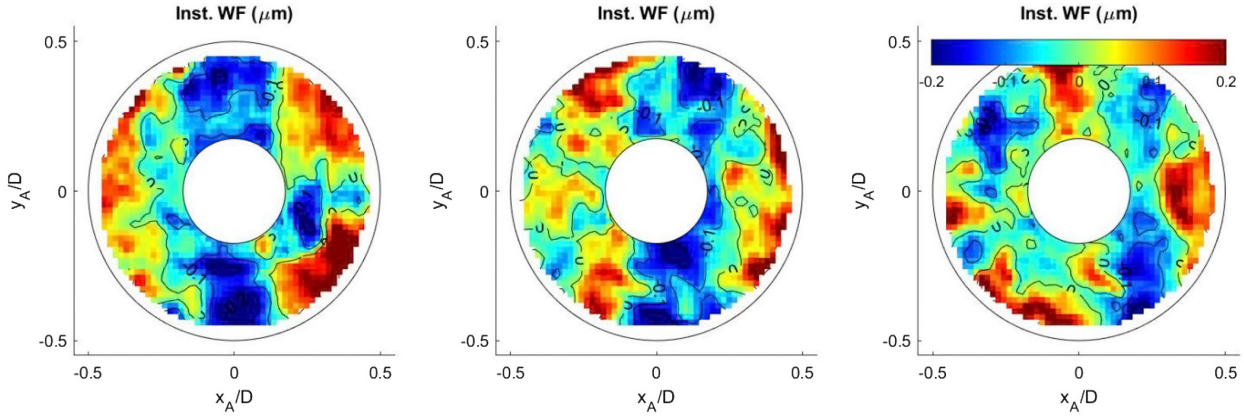

Fig. 4 Representative instantaneous wave fronts (labeled as Inst. WFs) collected through the shear layer downstream of the porous fence. Spatial coordinates are normalized by the beam diameter, $D = 0.2$ m. Incoming $M_\infty = 0.5$, flow goes from left to right.

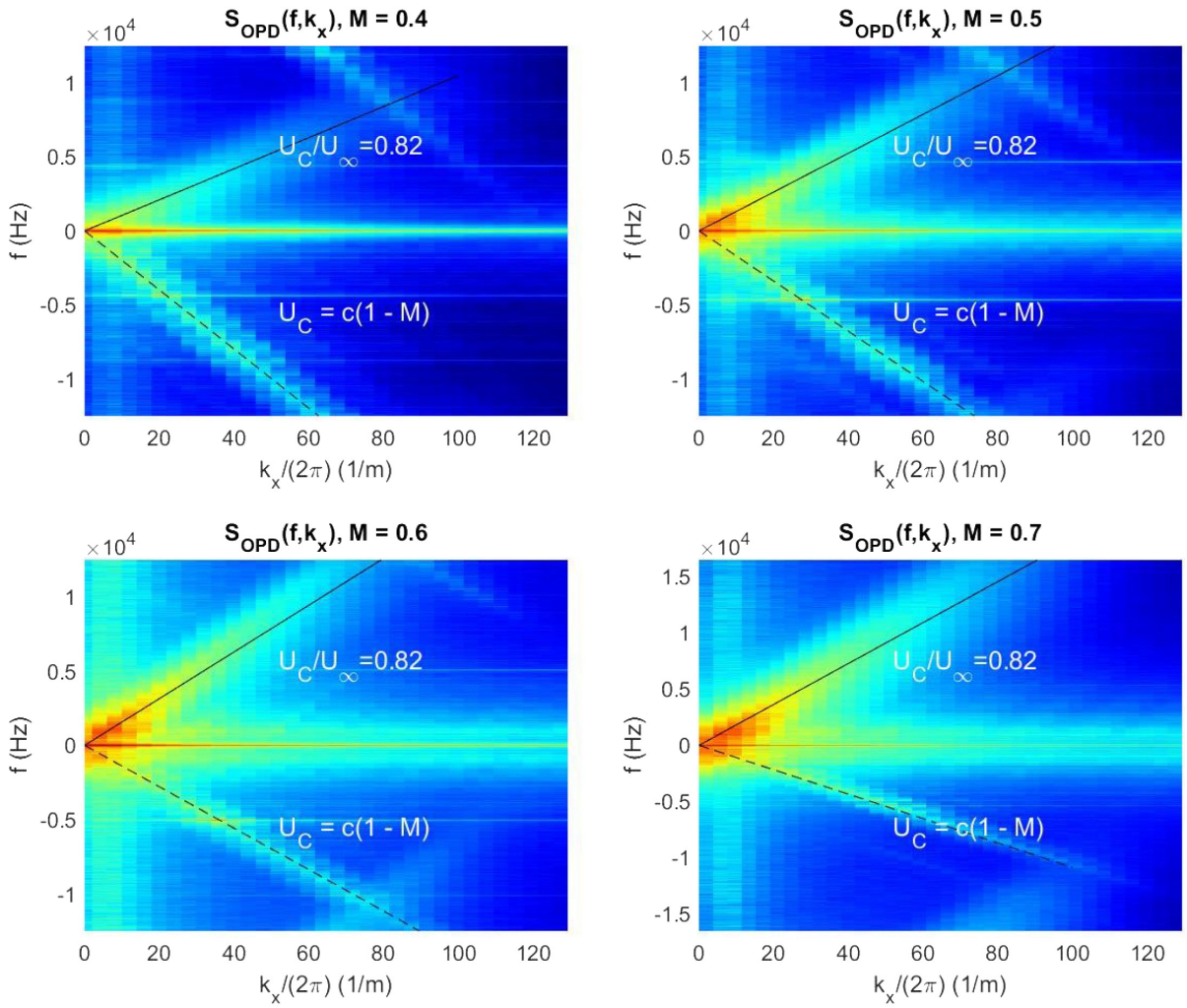

Fig. 5 Dispersion spectra, defined in Eq. (5), for the boundary-layer cases for all measured Mach numbers.

the wave fronts. While the steady-lensing (time-averaged) wave front was removed from the wave fronts, a small amount of the slowly changing residual defocus is still present. It will result in the presence of the third branch along $f = 0$, which can be observed in Fig. 5.

Two-dimensional dispersion spectra for the shear-layer cases are presented in Fig. 6 for all measured Mach numbers. The acoustic branch is clearly visible in the negative-frequency region at all Mach numbers with the slope also equal to the expected convective speed of $c(1 - M_\infty)$. The convective structure, related to the shear layer, is present in the spectra in the positive-frequency region, with the convective speed of approximately 0.85 of the freestream speed. As the shear layer is more optically distorting than the boundary layer, the downstream convecting branches in Fig. 6 are more energetic than the ones in Fig. 5. A detailed analysis of the aerooptical distortions due to the shear-layer structure can be found in [13].

The dispersion analysis can be used to separate the wave fronts into the corresponding upstream and downstream moving components by performing the inverse Fourier transform using either the downstream convecting ($f > 0, k_x > 0$) harmonics or the upstream-traveling harmonics ($f > 0, k_x < 0$) of the Fourier transform,

$$\mathrm{OPD}(t, x_A, y_A) = \mathrm{OPD}^{\mathrm{Down}}(t, x_A, y_A) + \mathrm{OPD}^{\mathrm{Up}}(t, x_A, y_A)$$
$$\mathrm{OPD}^{\mathrm{Down}}(t, x_A, y_A) = \frac{2}{(2\pi)^2} Re\left\{\int_0^\infty \int_0^\infty \int_{-\infty}^\infty \widehat{\mathrm{OPD}}(f, k_x, k_y) e^{i(2\pi f t - k_x x_A - k_y y_A)}\, \mathrm{d}f \mathrm{d}k_x\, \mathrm{d}k_y\right\}$$
$$\mathrm{OPD}^{\mathrm{Up}}(t, x_A, y_A) = \frac{2}{(2\pi)^2} Re\left\{\int_{-\infty}^0 \int_0^\infty \int_{-\infty}^\infty \widehat{\mathrm{OPD}}(f, k_x, k_y) e^{i(2\pi f t - k_x x_A - k_y y_A)}\, \mathrm{d}f \mathrm{d}k_x\, \mathrm{d}k_y\right\} \tag{7}$$

After separating the downstream- and upstream-traveling components for both the boundary-layer and shear-layer cases, the overall levels of $\mathrm{OPD}_{\mathrm{RMS}}$ of respective components were computed, as discussed before, and are presented in Fig. 7. The levels of $\mathrm{OPD}_{\mathrm{RMS}}$ of the downstream convecting aerooptical component, corresponding to either the boundary- or the shear-layer structures, are shown in Fig. 7a. The levels of aerooptical distortions increase with Mach number, since at subsonic speeds the aerooptical distortions are proportional to M_∞^2 [3,15,21]. As mentioned before, aerooptical distortions due to the shear layer are stronger than the distortions due to the boundary layer, which is evident in Fig. 7a.

The levels of aerooptical distortions due to the acoustic only component, shown in Fig. 7b, are approximately the same for both the boundary-layer and shear-layer cases and for almost all Mach numbers. Again, this is expected behavior, as unlike aerooptical structures, acoustically related distortions depend only on the noise intensity of the jet engine, which was approximately constant over the range of flight Mach numbers.

The spectrum for the shear-layer case at $M_\infty = 0.7$, see the bottom plot in Fig. 6, reveals that in the negative-frequency portion of the spectrum, which corresponds to the upstream-traveling structures, in addition to the acoustic branch, there are other energetic regions. One of them is between $k_x/(2\pi) = 0$ and 20 1/m, which corresponds to the spectral leakage from low frequencies. The second one is for $f < -5$ kHz and $k_x/(2\pi)$ between 40 and 801/m and is related to the spectral aliasing from the positive-frequency region of the spectrum. These additional energetic regions, related to the large-scale shear-layer structures, are responsible for the increase in the overall levels of the upstream-traveling component of $\mathrm{OPD}_{\mathrm{RMS}}$ at this speed, observed in Fig. 7b. Similar contaminations can also be observed in the boundary-layer data (see Fig. 5); however, as the boundary-layer structures are less energetic, compared to the shear-layer ones, they do not significantly affect the values of $\mathrm{OPD}_{\mathrm{RMS}}$ for the upstream-traveling component.

Note that by separating wave fronts into the downstream- and upstream-moving components, it is possible to study a much weaker upstream acoustic component which, if not separated, would otherwise be overwhelmed by a much stronger shear-layer-related aerooptical signal.

The aperture-averaged power spectra for both the downstream and upstream wave front components were computed for each case and at each Mach number. The resultant plots for the boundary-layer case

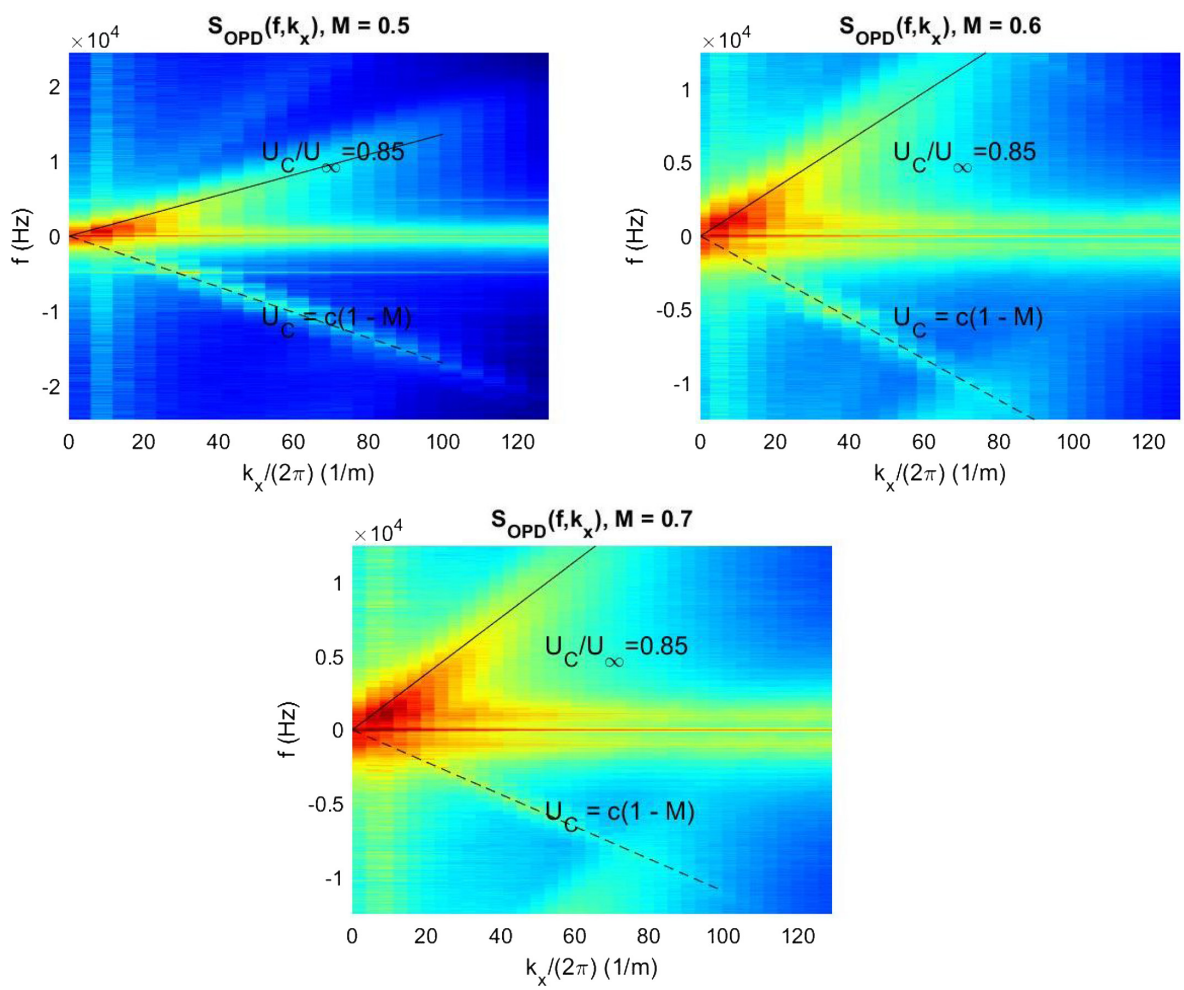

Fig. 6 Dispersion spectra, defined in Eq. (5), for SL cases for all measured Mach numbers.

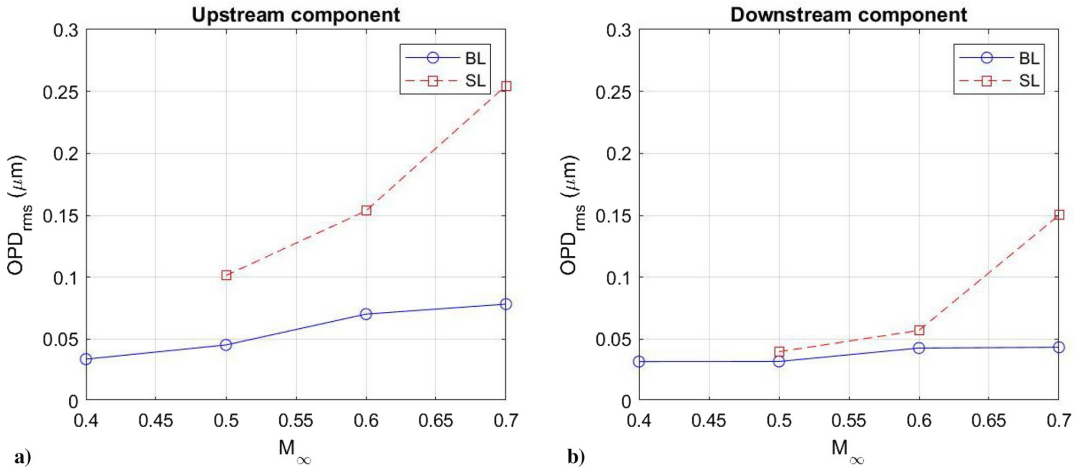

Fig. 7 Time-averaged a) OPD_{RMS}, corresponding to the upstream-traveling or convecting component for both BL and SL cases, and b) OPD_{RMS}, corresponding to the downstream-traveling or acoustic component for both the BL and SL cases.

can be seen in Fig. 8, with the frequency resolution of $\Delta f = 12$ Hz. The power spectra for the downstream component, presented in absolute units in Fig. 8a, show smooth shapes, expected from the turbulent boundary layer. Both the amplitude and location of the peak increase with Mach number, in agreement with previous studies [3]. For clarity, the spectra for the downstream component were replotted in normalized units, where the spectra were normalized by OPD^2_{RMS} and the frequency was normalized by the freestream speed U_∞ and the boundary-layer thickness δ as $St = f\delta/U_\infty$. The resultant normalized spectra are presented in Fig. 8b and indeed show the collapse of the spectra for all tested Mach numbers, except for $M = 0.4$. The normalized spectra are approximately constant up to $St = 0.3$ and then exhibit a monotonic decrease at higher frequencies. Numerical simulations of a canonical boundary-layer revealed a similar aeroptical spectra shape [22].

Similar features in the downstream spectra were observed for the shear-layer flows, shown in both absolute units; see Fig. 9a. The frequency resolution was the same as for the BL case. As for the BL case, the downstream components of the spectra for the SL case also exhibit a reasonable collapse of the spectra, presented in Fig. 9b, when plotted in the normalized units, using the shear-layer structure size Λ_{SL} as a characteristic length. The wave front spectra have a wide peak near $St = 0.6$, which is indicative of the regular, convecting shear-layer structures.

On the other hand, the acoustic-related spectra, shown in Figs. 8c and 9c, exhibit sharp and distinct tonal peaks near 5 kHz, which in

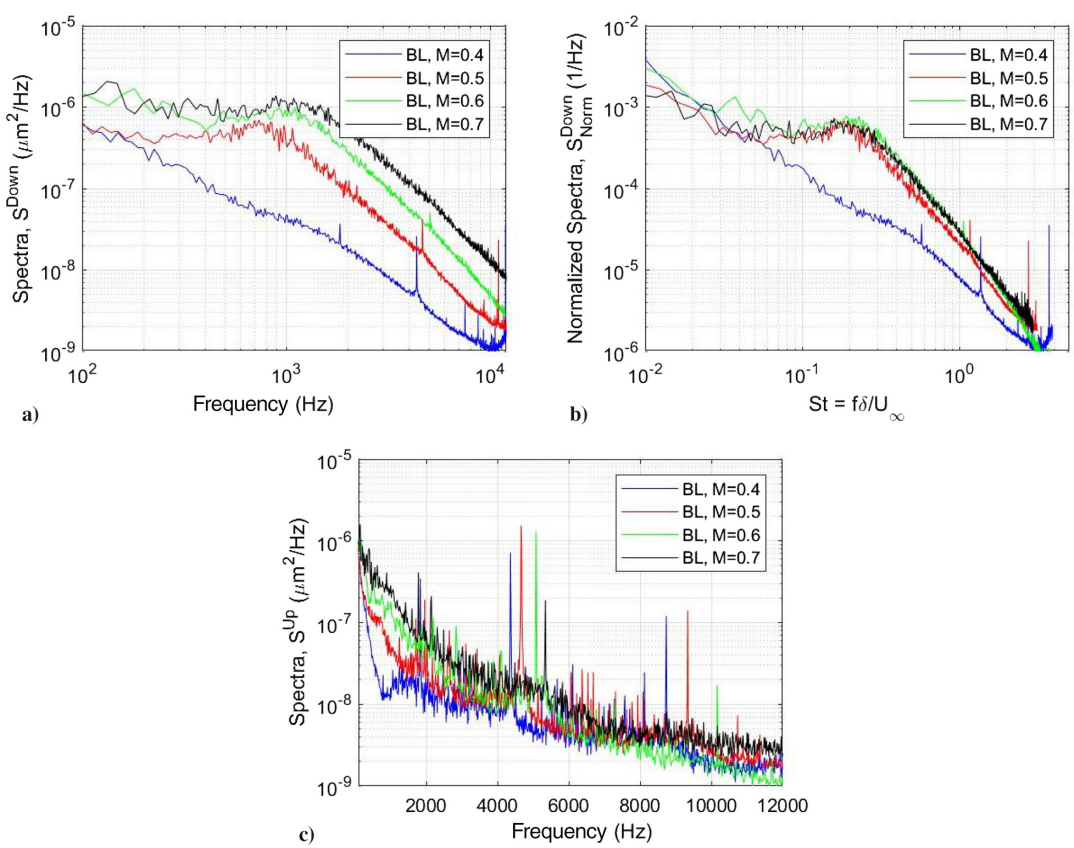

Fig. 8 Aperture-averaged spectra, defined in Eq. (6), for the downstream-convecting component in a) absolute units and in b) normalized units, with the normalized frequency, $St = f\delta/U_\infty$, and for c) upstream-moving acoustic component of the wave fronts for BL case for all measured Mach numbers.

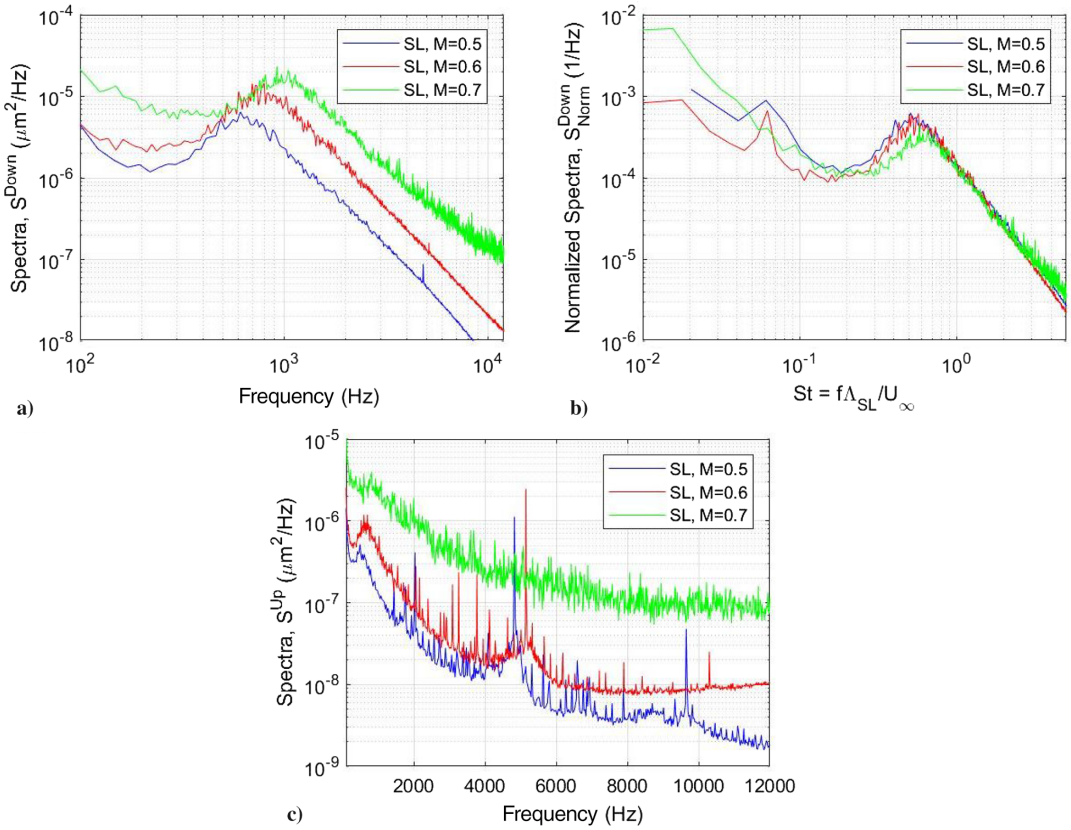

Fig. 9 Aperture-averaged spectra, defined in Eq. (6), for the downstream-convecting component in a) absolute units and in b) normalized units, with the normalized frequency, $St = f\Lambda_{SL}/U_\infty$, and for c) upstream-moving acoustic component of the wave fronts for the SL case for all measured Mach numbers.

previous studies [7] were linked to the blade pass frequency (BPF) of the engine fan. Other peaks near 10 kHz were identified as harmonics of the fundamental peaks. The exception is the acoustic-related spectrum for the shear-layer case at $M_\infty = 0.7$ in Fig. 9c, where no peaks were observed due to various contaminating sources affecting the extracted upstream spectrum, as discussed earlier. Using the spectra, the frequencies of the fundamental peaks for different Mach numbers were extracted and are given in Table 2. To confirm that these peaks are indeed BPFs, the actual rotations per minute of the engine fan were recorded in flight as a percentage of the manufacturer specified maximum rotations per minute of the Honeywell engine fans (equal to 11,502 rotations/ min) and also given in Table 2. As the engine fan has 30 blades, the expected BPFs were computed and are given in Table 2 as well. They agree with the measured peak frequencies with the relative difference of less than 2%, confirming that the dominant peaks in the acoustic-related spectra in Figs. 8c and 9c are indeed BPFs.

Representative dynamic modes, computed using the DFT algorithm, for the upstream-moving component of the wave fronts for the boundary-layer case at several selected frequencies, including the blade pass frequency, are shown in Fig. 10. These modes clearly show spanwise-uniform and streamwise-periodic structures, present not only at the strongest spectrum peak, corresponding to BPF, but at other frequencies as well. These periodic structures are resultant from the acoustic waves from the engine. Dynamic modes for the downstream-convecting component of the wave fronts at similar frequencies (not shown) do not exhibit any distinct spanwise-uniform features, as expected for turbulent flows.

Table 2 Measured and expected blade pass frequencies (BPF)

Tested cases	Measured BPF, Hz	Reported % of max rotations/min (11,502 rotations/min)	Expected BPF, Hz	Relative difference between BPFs, %
BL, $M_\infty = 0.4$	4363	77	4428	−1.5
BL, $M_\infty = 0.5$	4663	81	4658	−0.1
BL, $M_\infty = 0.6$	5085	90	5175	−1.7
BL, $M_\infty = 0.7$	5346	93	5348	0
SL, $M_\infty = 0.5$	4827	84	4830	0
SL, $M_\infty = 0.6$	5150	90	5175	−0.5 if

B. Analytical Modeling

To quantify how acoustic waves create aerooptical distortions, a simple omnidirectional single-frequency point source in a moving flow [23], located at a distance L upstream of the aperture, was used to model the engine fan noise. The related spatial–temporal acoustic pressure field was derived in [23] and is given in Eq. (8). The (x, y, z) frame of reference is chosen such that the source is located at the origin,

$$p'(x, y, z, t; f) = \frac{A}{4\pi R^*} \cos\left(2\pi f\left[t - \frac{(-M_\infty x + R^*)}{c(1 - M_\infty^2)}\right]\right)$$
$$\text{where } R^* = \sqrt{x^2 + (1 - M_\infty^2)(y^2 + z^2)} \tag{8}$$

Figure 11a shows the spatial distribution of the pressure field for a frequency of 500 Hz with the flow moving from left to right at $M_\infty = 0.5$. The spatial wavelength of the acoustic field, $\Lambda = U_C/f$, is smaller upstream of the source and larger downstream of it. Since the frequency of the acoustic source stays the same, the wavelength will depend on the aircraft speed, since the observed convective velocity of wave propagation in the aircraft frame of reference is either $U_C^{Up} = U_\infty - c = -c(1 - M_\infty)$ or $U_C^{Down} = U_\infty + c = c(M_\infty + 1)$.

When the laser beam propagates through the acoustic field in the z direction along the dashed line in Fig. 11a, it crosses regions of positive and negative pressures induced by the acoustic waves. The laser beam travels through a region of approximately constant

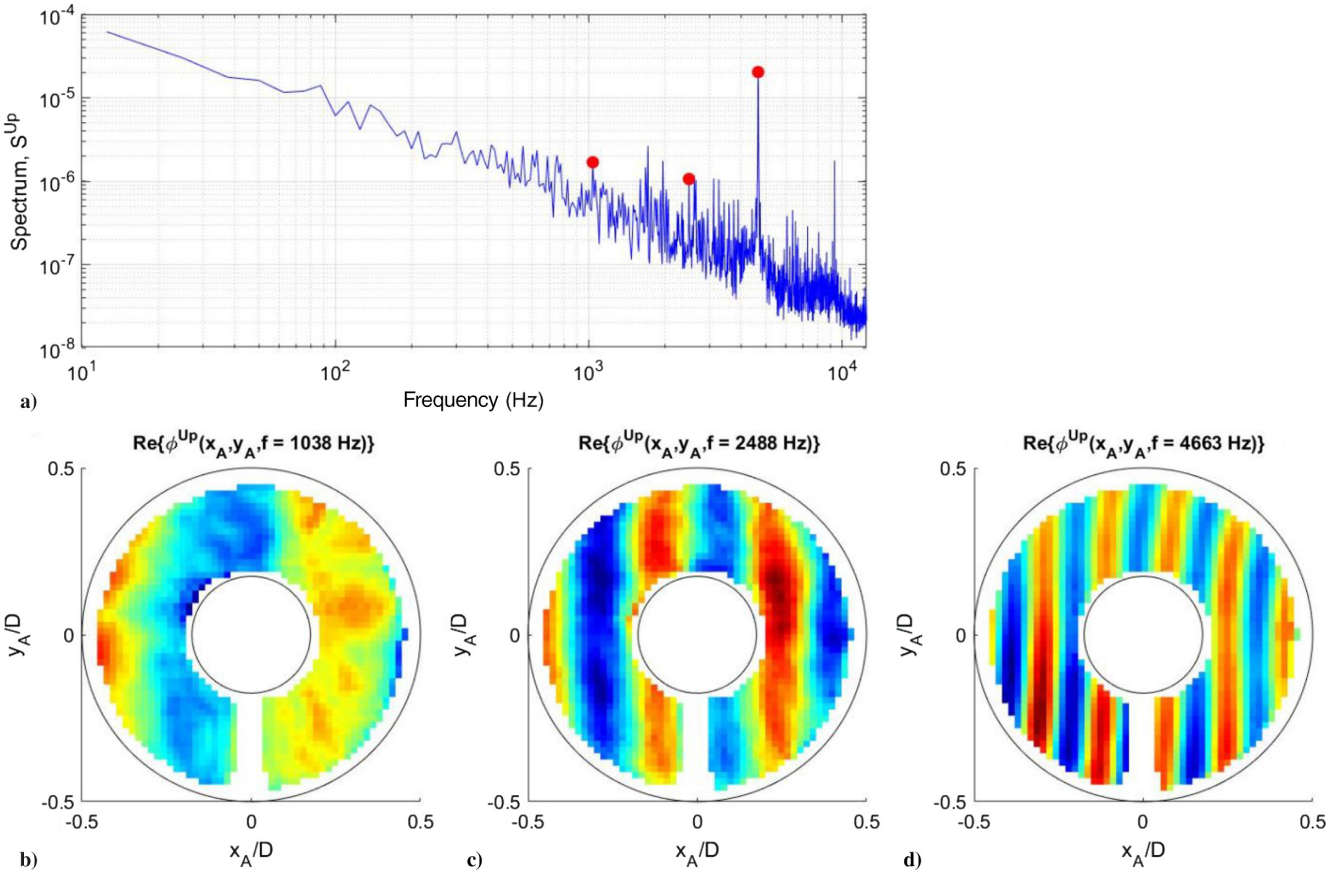

Fig. 10 a) DMD spectrum, defined in Eq. (6), for the upstream-moving distortions for the BL case, $M_\infty = 0.5$. b–d). Real parts of spatial dynamic modes, corresponding to the frequencies, labeled as red circles in part a.

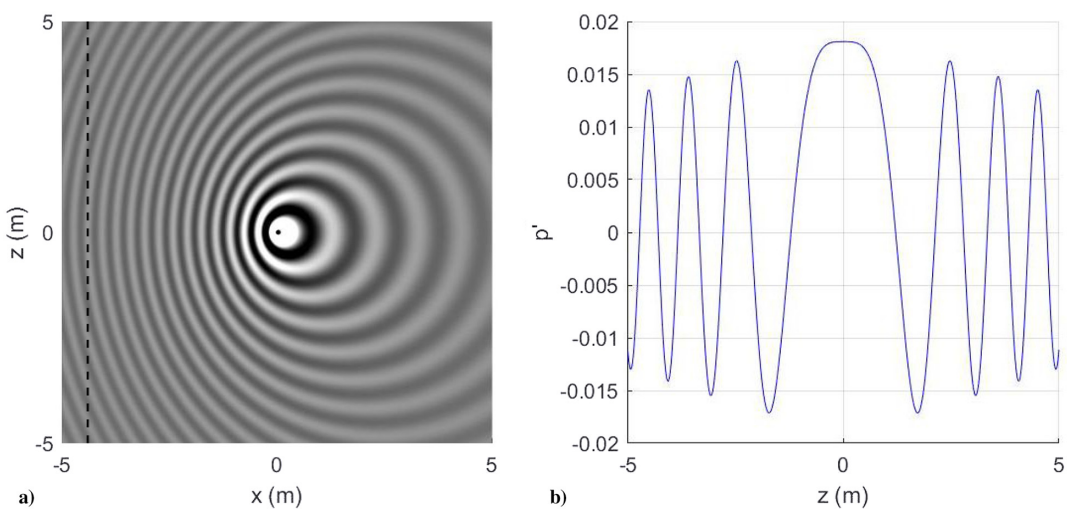

Fig. 11 a) Spatial variation of the acoustic pressure field along the x–z plane, defined in Eq. (8), for $f = 500$ Hz in the moving flow with $M_\infty = 0.5$. Flow goes from left to right. b) Acoustic pressure field along the dashed line in z direction, indicated in part a.

pressure only in the region near $z = 0$. The z dependence of the pressure field is presented in Fig. 11b, where the pressure variation along the dashed line, indicated in Fig. 11a, is plotted. The pressure is roughly constant for -0.5 m < z < 0.5 m, but starts rapidly oscillating outside of this region.

The density and pressure in the acoustic field are linearly related via the adiabatic relationship, Eq. (2), which can be rewritten as $p' = \rho' c^2$. Therefore, the pressure field can be integrated along z lines to compute the resultant OPD field as a function of (x, y) locations and time,

$$\mathrm{OPD}(x,y,t;f) = \int_{-\infty}^{\infty} n'(x,y,z,t;f)\,\mathrm{d}z = K_{\mathrm{GD}} \int_{-\infty}^{\infty} \rho'(x,y,z,t;f)\,\mathrm{d}z = \frac{K_{\mathrm{GD}}}{c^2} \int_{-\infty}^{\infty} p'(x,y,z,t;f)\,\mathrm{d}z \tag{9}$$

As discussed before, while OPD is technically an integral quantity, most of the contribution to the integral in Eq. (9) comes from the region near $y = z = 0$, where pressure stays approximately constant. Outside of this region, the rapidly oscillating pressure field mostly

cancels itself in the integral, resulting in only a small contribution to OPD. Thus, OPD is primarily sensitive to the pressure variations at the region near $y = z = 0$. Defining this region as the region where the quantity in the cosine term in Eq. (8) is less than $\pi/2$, the region extent where the pressure is approximately constant can be found as $|y, z| \leq \sqrt{Lc/(2f)}$. It can be seen that the region becomes more compact for high frequencies. Therefore, the integral quantity $\mathrm{OPD}(x, y, t)$ can be used to estimate the local pressure near $y = z = 0$. Using Eq. (8), the pressure variations at $y = z = 0$ become

$$p'(x, y = 0, z = 0, t; f) = \frac{A}{4\pi|x|}\cos\left(2\pi f\left[t + \frac{x}{c(1 - M_\infty)}\right]\right) \tag{10}$$

which corresponds to the upstream-traveling wave with the observed convective speed of $U_C = c(1 - M_\infty)$.

For infinite z limits, the integration in Eq. (9) can be carried out analytically to get the following expression,

$$\mathrm{OPD}(x, y, t; f) = \frac{AK_{\mathrm{GD}}}{c^2}\frac{1}{4\sqrt{1 - M_\infty^2}}[\sin(\varphi)J_0(\xi) - \cos(\varphi)Y_0(\xi)], \text{ where}$$
$$\varphi = 2\pi f\left(t + \frac{M_\infty x}{c(1 - M_\infty^2)}\right), \quad \xi = \frac{2\pi f\sqrt{x^2 - (1 - M_\infty^2)y^2}}{c(1 - M_\infty^2)} \tag{11}$$

and J_0 and Y_0 are Bessel functions of first and second kinds, respectively.

As the beam aperture is located upstream of the point source, the relationship between streamwise coordinates for the aperture and the noise source is $x = x_A - L$. For aperture diameters which are small relative to the distance to the acoustic source, $D/L \ll 1$, the y term in ξ value in Eq. (11) is much smaller in amplitude than the first term, which is $x \approx -L$, giving $\xi \approx (2\pi fL/c(1 - M_\infty^2))$. For large ξ values, corresponding to either large L and/or high frequencies, Eq. (11) can be asymptotically expanded to become

$$\mathrm{OPD}(x_A, y_A, t; f) \approx \frac{AK_{\mathrm{GD}}}{4\pi c^2}\sqrt{\frac{c}{fL}}\cos\left(2\pi f\left[t + \frac{x_A - L}{c(1 - M_\infty)}\right] - \frac{\pi}{4}\right),$$
$$\frac{2\pi fL}{c(1 - M_\infty^2)} \geq 2 \tag{12}$$

This equation represents the wave fronts, spatially varying only in the streamwise direction and traveling upstream with the convective speed of $U_C = c(1 - M_\infty)$. Experimentally observed dynamic modes in Fig. 10 have the same spatial features, validating the assumption that the engine noise generation can be reasonably approximated by a point acoustic source. Comparing Eq. (10) and Eq. (12), it can be seen that both the pressure fluctuations and the wave fronts have the same traveling term, with the wave fronts lagging the pressure fluctuations by $\pi/4$.

Since both Eq. (10) and Eq. (12) are given for a single frequency, the coefficients in front of the cosine terms in these equations can be treated as amplitudes of the Fourier harmonics at the same frequency. Thus, the ratio between the harmonic energies, which are simply amplitude squares, would give the transfer function, relating aerooptical and pressure power spectra. Before deriving this transfer function, recall that instantaneous piston and tip/tilt components are removed from the individual wave fronts before any data reduction and the aerooptical spectrum is computed as aperture-averaged amplitude- squares of the dynamic modes [see data reduction section and Eq. (6)]. As demonstrated in [16,24], the removal of the instantaneous piston and tip/tilt will result in reducing the overall $\mathrm{OPD}_{\mathrm{RMS}}$ of the single-frequency traveling harmonic and can be expressed as the aperture transfer function, $(\overline{\mathrm{OPD}_{\mathrm{RMS}}^2(D/\Lambda)})/\overline{\mathrm{OPD}_{\mathrm{RMS}}^2(D = \infty)} = G(D/\Lambda)$, where Λ is the wave front wavelength and the overbar denotes time averaging. For circular apertures and traveling harmonics in the form of spanwise-uniform waves in the form of $\cos(2\pi f[t - x/U_C])$, the wavelength is related to the frequency as $\Lambda = U_C/f$, and the G function has an analytical representation [16],

$$G(\eta = D/\Lambda = fD/U_C) = 1 - \frac{16J_0^2(\pi\eta) + 4J_1^2(\pi\eta)}{(\pi\eta)^2} + \frac{64J_0(\pi\eta)J_1(\pi\eta)}{(\pi\eta)^3} - \frac{64J_1^2(\pi\eta)}{(\pi\eta)^4} \tag{13}$$

where J_0 and J_1 indicate Bessel functions of the first kind. The G function is plotted in Fig. 12.

In the flight experiments, the engine is located at $z_1 = 0.54$ m away from the aircraft fuselage, and technically the integration in Eq. (9) should be performed from $-z_1$ to infinity. But possible sound reflections from the aircraft fuselage should be considered. If the fuselage is replaced with a flat wall, spanned in the x–y plane with a full reflection, it is straightforward to demonstrate that the resultant sound field and the optical distortions will be exactly the same as for the inbounded space (that is, no wall). In reality of course, the fuselage is a cylindrical body. However, the deviations of the real acoustic field with the included reflection from the cylindrical fuselage will be sufficiently small, especially for high frequencies. Thus, the infinite space G function, given by Eq. (13), can still be used as an approximation of the real G function.

Using the aperture transfer function $G(fD/U_C)$, given in Fig. 12, and Eqs. (10) and (12), the relationship between the acoustic component of piston/tilt-removed aperture averaged OPD spectrum $S^{\mathrm{Up}}(f)$, defined either in Eq. (6) or calculated using the acoustic-only component of OPD in Eq. (7), and the acoustic pressure power spectrum $S_p(f)$ at the point ($x_A = y_A = z = 0$) can finally be established and is shown in Eq. (14),

$$\frac{S^{\mathrm{Up}}(f)}{S_p(f)} = \frac{K_{\mathrm{GD}}^2 L}{c^3 f} \cdot G(fD/U_C) \tag{14}$$

Equation (14) can be used to estimate aerooptical distortions from the engine noise if the acoustic spectrum is known. Conversely, the acoustic component of the aerooptical spectrum can be used to estimate the acoustic pressure spectrum. Using the aerooptical spectra from Figs. 8c and 9c, the resultant acoustic pressure spectra for both the boundary-layer and shear-layer cases for all Mach numbers are presented in Fig. 13. Except for the highest Mach number of $M_\infty = 0.7$ for the shear-layer case, the acoustic pressure spectra look very similar for all other cases and Mach numbers, with the main peaks related to the blade pass frequency and their harmonics. In addition to the sharp peaks, the spectra also have a significant low-frequency broadband component below 500 Hz. Analysis of dynamic modes at these low frequencies (not shown) revealed that the low end is contaminated by the convecting flow structure. This contaminating effect can also be observed in the dispersion plots in Figs. 5 and 6. Therefore, the observed increase in the acoustic

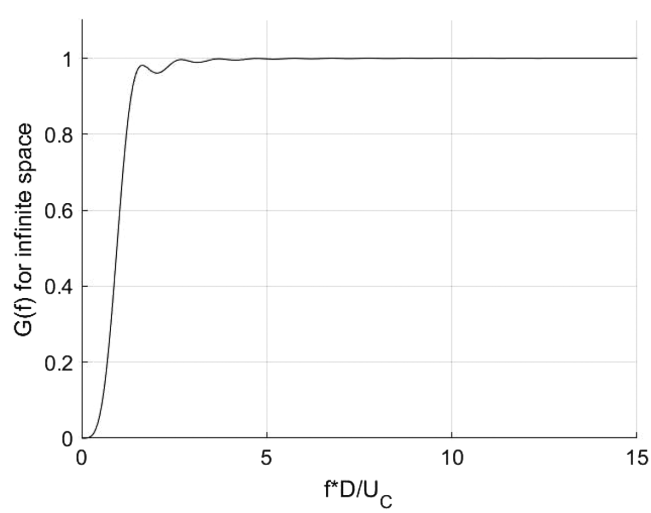

Fig. 12 Aperture transfer function for the acoustic source for the infinite space, Eq. (13).

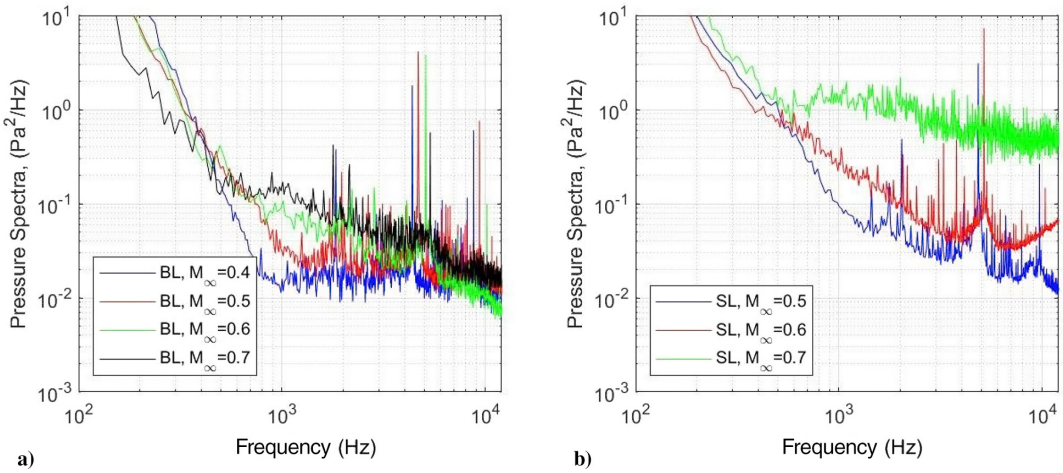

Fig. 13 Estimated acoustic pressure spectra for a) BL and b) SL cases for measured Mach numbers.

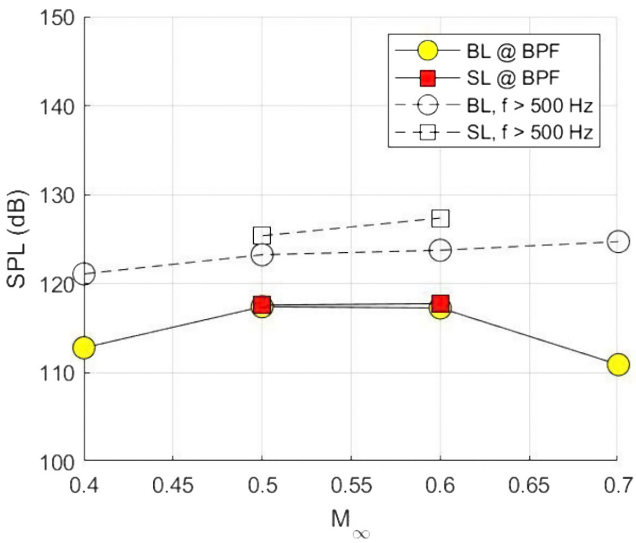

Fig. 14 Estimated SPL for $P_{\mathrm{ref}} = 20\ \mu$Pa for the tonal noise at the blade pass frequencies and the broadband noise for frequencies above 500 Hz.

pressure spectra at low frequencies below 500 Hz in Fig. 13 is not related to the actual acoustic pressure spectra and should be ignored.

The estimated acoustic pressure spectra in Fig. 13 can be used to compute SPLs, with the reference sound pressure $P_{\mathrm{ref}} = 20\ \mu$Pa, for the tonal noise near the blade pass frequency and for the broadband noise for frequencies above 500 Hz. The resultant SPLs in decibels are shown in Fig. 14 for both the boundary-layer and shear-layer cases. The tonal SPL is approximately 115 dB over the range of Mach numbers tested. SPLs for both the boundary-layer and shear-layer cases are very similar, confirming the ability of the presented analysis to decouple, isolate, and study solely the acoustic component of the wave fronts. While direct acoustic measurements from the engine in flight were not performed, the computed tonal SPL is consistent with the previous estimates of the tonal SPL approximately 117 dB [7]. The broadband SPLs are about 125 dB for all measured Mach numbers and are largely independent of the type of turbulent flow over the aperture.

V. Conclusions

Wave front measurements were performed in flight at varying subsonic Mach numbers through both a natural boundary layer and an artificially introduced shear-layer environment on AAOL-BC. Sound waves radiating from the aircraft's engine fan located downstream of the measurement window induced upstream-moving optical distortions in all collected wave front data. Dispersion analysis was used to decouple and calculate the power spectra and the convective speeds of both aerooptical- and acoustic-related distortions. It was found that, while the levels of the aerooptical component, related to either the boundary layer or shear layer, increase with the Mach number, the acoustic-related component was approximately the same for almost all tested Mach numbers. Analysis of the acoustic-only spectra revealed the presence of a strong tone with its harmonics, and it was shown that this tone coincides with the blade pass frequency of the engine fan. The speed of the upstream-traveling component was found to be the difference between the speed of sound and the speed of the aircraft, as predicted by the theory. Dynamic mode decomposition analysis was also employed to confirm that the spectral peaks seen in the upstream-traveling component of the wave front data do in fact correspond to the blade pass frequency of the jet engine. The dominant dynamic modes revealed spanwise-uniform and streamwise-periodic structures indicative of these acoustic waves, emitted by the engine fan.

An analytical model was proposed to quantify how acoustic waves create aerooptical distortions. Modeling the noise of the engine fan as a point omnidirectional acoustic source, it was shown that the largest contribution to the acoustic-related optical distortions comes from a compact region in the immediate vicinity of the measurement window. It allows relating the global optical distortions to the local pressure fluctuations. Using this notion, a transfer function was derived relating the acoustic pressure spectrum to the upstream-traveling acoustic component of the aerooptical spectrum. This transfer function can be used to either estimate the contaminating effect of the engine noise on the overall aerooptical distortions in realistic flight conditions or, conversely, to estimate the sound-related unsteady pressure fluctuations and sound pressure levels from the wave front measurements.

Acknowledgments

This Paper is supported by the Joint Technology Office, grant number FA9550-13-1-0001, and Office of Naval Research, grant number N00014-18-1-2112.

References

[1] Wang, M., Mani, A., and Gordeyev, S., "Physics and Computation of Aero-Optics," *Annual Review of Fluid Mechanics*, Vol. 44, No. 1, 2012, pp. 299–321. https://doi.org/10.1146/annurev-fluid-120710-101152

[2] Jumper, E. J., and Gordeyev, S., "Physics and Measurement of Aero-Optical Effects: Past and Present," *Annual Review of Fluid Mechanics*, Vol. 49, No. 1, 2017, pp. 419–441. https://doi.org/10.1146/annurev-fluid-010816-060315

[3] Gordeyev, S., Smith, A. E., Cress, J. A., and Jumper, E. J., "Experimental Studies of Aero-Optical Properties of Subsonic Turbulent

Boundary Layers," *Journal of Fluid Mechanics*, Vol. 740, 2014, pp. 214–253.
https://doi.org/10.1017/jfm.2013.658

[4] Catron, B., Rennie, R. M., Gordeyev, S., and Jumper, E. J., "Effect of Acoustic Disturbances on Aero-Optical Measurements," AIAA Paper 2018-3903, 2018.
https://doi.org/10.2514/6.2018-3903

[5] Catron, B. L., Rennie, M. R., Gordeyev, S., and Jumper, E. J., "Filtering of Acoustic Disturbances from Aero-Optical Measurements," AIAA Paper 2020-0683, 2020.
https://doi.org/10.2514/6.2020-0683

[6] Hugo, R. J., Nowlin, S. R., Hahn, I. L., Eaton, F. D., and McCrae, K. A., "Acoustic Noise-Source Identification in Aircraft-Based Atmospheric Temperature Measurements," *AIAA Journal*, Vol. 40, No. 7, 2002, pp. 1382–1387.
https://doi.org/10.2514/2.1798

[7] De Lucca, N., Gordeyev, S., Jumper, E., and Wittich, D. J., "Effects of Engine Acoustic Waves on Optical Environment Around Turrets In-Flight on AAOL-T," *Optical Engineering*, Vol. 57, No. 6, June 2018, Paper 064107.
https://doi.org/10.1117/1.OE.57.6.064107

[8] Jumper, E. J., Zenk, M., Gordeyev, S., Cavalieri, D., and Whiteley, M., "Airborne Aero-Optics Laboratory," *Journal of Optical Engineering*, Vol. 52, No. 7, 2013, Paper 071408.
https://doi.org/10.1117/1.OE.52.7.071408

[9] Jumper, E. J., Gordeyev, S., Cavalieri, D., Rollins, P., Whiteley, M. R., and Krizo, M. J., "Airborne Aero-Optics Laboratory-Transonic (AAOL-T)," AIAA Paper 2015-0675, 2015.
https://doi.org/10.2514/6.2015-0675

[10] Porter, C., Gordeyev, S., Zenk, M., and Jumper, E. J., "Flight Measurements of the Aero-Optical Environment Around a Flat-Windowed Turret," *AIAA Journal*, Vol. 51, No. 6, 2013, pp. 1394–1403.
https://doi.org/10.2514/1.J052067

[11] De Lucca, N., Gordeyev, S., and Jumper, E. J., "In-Flight Aero-Optics of Turrets," *Journal of Optical Engineering*, Vol. 52, No. 7, 2013, Paper 071405.
https://doi.org/10.1117/1.OE.52.7.071405

[12] Morrida, J., Gordeyev, S., De Lucca, N., and Jumper, E. J., "Shock-Related Effects on Aero-Optical Environment for Hemisphere-On-Cylinder Turrets at Transonic Speeds," *Applied Optics*, Vol. 56, No. 16, 2017, pp. 4814–4824.
https://doi.org/10.1364/AO.56.004814

[13] Kalensky, M., Gordeyev, S., and Jumper, E. J., "In-Flight Studies of Aero-Optical Distortions Around AAOL-BC," AIAA Paper 2019-3253, 2019.
https://doi.org/10.2514/6.2019-3253

[14] Gordeyev, S., Burns, W. R., Jumper, E., Gogineni, S., Paul, M., and Wittich, D. J., "Aero-Optical Mitigation of Shocks Around Turrets at Transonic Speeds Using Passive Flow Control," AIAA Paper 2013-0717, 2013.
https://doi.org/10.2514/6.2013-717

[15] Kemnetz, M., "Analysis of the Aero-Optical Component of Jitter Using the Stitching Method," Ph.D. Dissertation, Univ. of Notre Dame, Notre Dame, IN, 2019.

[16] Siegenthaler, J. P., "Guidelines for Adaptive Optic Correction Based on Aperture Filtration," Ph.D. Dissertation, Univ. of Notre Dame, Notre Dame, IN, 2009.

[17] Taira, K., Brunton, S. L., Dawson, S. T. M., Rowley, C. W., Colonius, T., McKeon, B. J., Schmidt, O. T., Gordeyev, S., Theofilis, V., and Ukeiley, L. S., "Modal Analysis of Fluid Flows: An Overview," *AIAA Journal*, Vol. 55, No. 12, 2017, pp. 4013–4041.
https://doi.org/10.2514/1.J056060

[18] Schmid, P. J., "Dynamic Mode Decomposition of Numerical and Experimental Data," *Journal of Fluid Mechanics*, Vol. 656, Aug. 2010, pp. 5–28.
https://doi.org/10.1017/S0022112010001217

[19] Chen, K. K., Tu, J. H., and Rowley, C. W., "Variants of Dynamic Mode Decomposition: Boundary Condition, Koopman, and Fourier Analyses," *Journal of Nonlinear Science*, Vol. 22, No. 6, 2012, pp. 887–915.
https://doi.org/10.1007/s00332-012-9130-9

[20] Fitzgerald, E. J., and Jumper, E. J., "The Optical Distortion Mechanism in a Nearly Incompressible Free Shear Layer," *Journal of Fluid Mechanics*, Vol. 512, 2004, pp. 153–89.
https://doi.org/10.1017/S0022112004009553

[21] Gordeyev, S., and Jumper, E., "Fluid Dynamics and Aero-Optics of Turrets," *Progress in Aerospace Sciences*, Vol. 46, No. 8, 2010, pp. 388–400.
https://doi.org/10.1016/j.paerosci.2010.06.001

[22] Wang, K., and Wang, M., "Aero-Optics of Subsonic Turbulent Boundary Layers," *Journal of Fluid Mechanics*, Vol. 696, 2012, pp. 122–151.
https://doi.org/10.1017/jfm.2012.11

[23] Blokhintsev, D., "*Acoustics of a Nonhomogeneous Moving Medium*," NACA TM-1399, 1956.

[24] Siegenthaler, J., Gordeyev, S., and Jumper, E., "Shear Layers and Aperture Effects for Aero-Optics," AIAA Paper 2005-4772, 2005.
https://doi.org/10.2514/6.2005-4772

L. Ukeiley
Associate Editor